




Elasto-viscoplastic spreading: From plastocapillarity to elastocapillarity

Hugo L. França ¹, Maziyar Jalaal ^{2,*}, and Cassio M. Oishi ³

¹*Instituto de Ciências Matemáticas e Computação, Universidade de São Paulo, São Carlos 13566-590, Brazil*

²*Van der Waals-Zeeman Institute, Institute of Physics, University of Amsterdam, Amsterdam 1098 XH, Netherlands*

³*Departamento de Matemática e Computação, Faculdade de Ciências e Tecnologia, Universidade Estadual Paulista “Júlio de Mesquita Filho”, Presidente Prudente 19060-900, Brazil*



(Received 11 June 2023; accepted 22 December 2023; published 1 March 2024)

We study the spreading of elasto-viscoplastic (EVP) droplets under surface tension effects. The non-Newtonian material flows like a viscoelastic liquid above the yield stress and behaves like a viscoelastic solid below it. Hence, the droplet initially flows under surface tension forces but eventually reaches a final equilibrium shape when the stress everywhere inside the droplet falls below the resisting rheological stresses. We use numerical simulations and combine volume-of-fluid (VOF) method and an EVP constitutive model to systematically study the dynamics of spreading and the final shape of the droplets. The spreading process explored in this study finds applications in coating, droplet-based inkjet printing, and 3D printing, where complex fluids such as paints, thermoplastic filaments, or bio-inks are deposited onto surfaces. Additionally, the computational framework enables the study of a wide range of multiphase interfacial phenomena, from elastocapillarity to plastocapillarity.

DOI: [10.1103/PhysRevResearch.6.013226](https://doi.org/10.1103/PhysRevResearch.6.013226)

I. INTRODUCTION

The deposition and spreading of fluids over surfaces occur in a wide range of industrial applications, such as spray coating and printing [1–5]. The fluids used in these applications often contain microscopic constituents like polymers or colloids, resulting in highly nonlinear macroscopic rheological features like elasticity, plasticity, and shear-dependent viscosity. Hence, understanding the rheological effects on the fluid mechanics of spreading is essential for further optimizing current systems or designing new materials for specific applications [6]. In the past few years, many studies have investigated the impact and spreading of droplets on surfaces for fluids with various rheological properties, including viscous fluids [7–10], viscoelastic fluids [11–15], and yield stress materials [16–25]. However, systematic experiments are generally complicated due to the high-dimensional interconnected parameter space. To this end, computer simulations can be employed to investigate the significance of rheological parameters independently from one another.

Our focus will be on a general class of nonlinear materials named elasto-viscoplastic (EVP) fluids, which can exhibit both elastic and plastic properties, as well as viscous behavior. Many models of EVP fluids have been proposed

previously. Saramito [26,27] presented a description of EVP constitutive equations, which combine classical viscoplastic models (Bingham or Herschel-Bulkley) with viscoelastic models (Oldroyd-B or PTT). Adopting a different perspective, de Souza Mendes [28] used a generalized viscoelastic model where material properties are functions of the strain rate in order to incorporate the yielding behavior as well as the thixotropic effects. Dimitriou and McKinley [29] included isotropic and kinematic hardening in their EVP formulation to capture various steady and unsteady flow responses. Recent reviews of the development and thorough comparison of different EVP models can be found in Fragedakis *et al.* [30] and Saramito and Wachs [31], where they comment both on the mathematical/physical properties of the models, as well as the numerical characteristics. Moreover, many recent studies have incorporated the models above into computational frameworks to study various fluid dynamics problems such as flow around particles [32–34], flow in channels [35–37], flow in porous media [38,39], and flow around bubbles [40,41]. More related to the present investigations are the computational studies on droplets with EVP properties. Oishi *et al.* [20] studied the flow of materials on an inclined plane, considering elastic properties, where they captured the so-called avalanche effect where a decrease in viscosity (triggered by a stress field) induces a motion that successfully creates another decrease in viscosity. In follow-up studies, Oishi *et al.* [22,42] have also included surface tension and thixotropic effects on the impact of EVP droplets on normal and inclined solid surfaces. Izbassarov and Tamissola [43] investigated how an EVP droplet deforms inside a Newtonian medium under simple shear and observe that the droplet deformation can present a nonmonotonic behavior as elasticity is changed.

*m.jalaal@uva.nl

Published by the American Physical Society under the terms of the [Creative Commons Attribution 4.0 International license](https://creativecommons.org/licenses/by/4.0/). Further distribution of this work must maintain attribution to the author(s) and the published article's title, journal citation, and DOI.

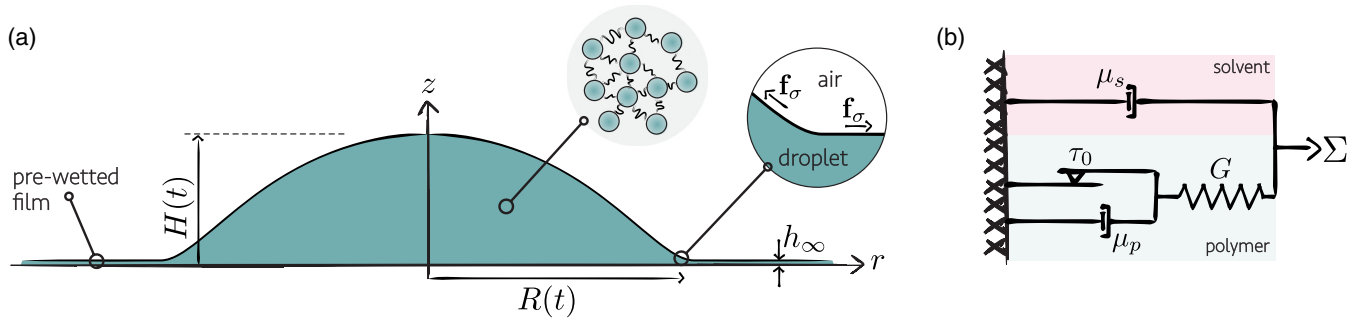


FIG. 1. (a) Sketch of the geometry of a spreading elasto-viscoplastic droplet. We assume the droplet to be axisymmetric around the z axis and spread on a thin prewetted film of the same material with thickness h_∞ . The radius and the height of the droplet are denoted respectively as $R(t)$ and $H(t)$. Gravity is neglected, hence, the spreading is purely due to surface tension effects. The droplet includes microscopic constituents, resulting in macroscopic EVP models. (b) Mechanical analog of Saramito's EVP model.

In the present paper, our main goal is to study the spreading of EVP droplets on a surface. To this end, we aim to extend the previous numerical analysis [44] to consider not only viscoplastic rheology, but also the addition of elasticity. By using Saramito's EVP model [26], a parametric study will be carried over in order to understand how the addition of elasticity can affect the transient spreading dynamics and also the final shapes of elasto-viscoplastic droplets.

The paper is organized as follows. Section II presents a description of the problem, the governing equations used to model the flow and the rheology of the EVP material, and also an overview of the numerical method used in this paper. In Sec. III, results are presented and various limits of the problem are visited. Section IV concludes the results and presents future perspectives. Additional numerical details can be found in the Appendices.

II. PROBLEM DESCRIPTION AND THE NUMERICAL FRAMEWORK

A. Problem description: Capillary spreading of a droplet

We consider the spreading of an axisymmetric EVP droplet on a wetted surface. The choice of geometry has two main reasons. Firstly, in several applications, including 3D printing and spray coating, it is typical for droplets to spread and deposit on an existing layer of the same fluid [9,10]. Secondly, opting for a geometry that eliminates the presence of a triple contact line provides theoretical and computational advantages as it simplifies the associated complex physics related to boundary conditions and stress singularities.

As illustrated in Fig. 1(a), a droplet is initially placed over a thin film of the same material and allowed to spread due to capillary forces. Viscous forces oppose this spreading by slowing it down, and yield stress is capable of stopping it completely as shown previously in [44] for a purely viscoplastic scenario. The role of elasticity in this process, however, is less clear and a numerical framework will be implemented in order to understand such effects. To this end, we will model the rheology of the EVP material by the Saramito model [26,27], which generalizes both the Bingham viscoplastic and the Oldroyd-B viscoelastic models. Figure 1(b) shows a mechanical analog of this model. Below the yield stress the material

behaves like a Kelvin-Voigt solid, while after yielding it flows as an Oldroyd-like fluid.

B. Governing equations

The governing equations for the isothermal incompressible bi-phase flow, are the continuity and momentum conservation given by

$$\nabla \cdot \mathbf{u} = 0, \quad (1)$$

$$\rho \left(\frac{\partial \mathbf{u}}{\partial t} + \nabla \cdot (\mathbf{u}\mathbf{u}) \right) = -\nabla p + \nabla \cdot \boldsymbol{\tau} + \mathbf{f}_g + \mathbf{f}_\sigma, \quad (2)$$

where \mathbf{u} and p are the velocity and pressure fields. The gravitational force is defined as $\mathbf{f}_g = \rho \mathbf{g}$ where ρ is the fluid mass density. In our numerical method, the surface tension force is also defined as a body force $\mathbf{f}_\sigma = \sigma \kappa \delta_s \mathbf{n}$, where κ is the curvature of the interface, σ the constant surface tension coefficient, \mathbf{n} is the unit vector normal to the interface, and δ_s is the Dirac delta function centered on the interface [45].

The deviatoric stress tensor $\boldsymbol{\tau}$ is the sum of the solvent $\boldsymbol{\tau}^s$ and polymeric $\boldsymbol{\tau}^p$ contributions,

$$\boldsymbol{\tau} = \boldsymbol{\tau}^s + \boldsymbol{\tau}^p. \quad (3)$$

The solvent stress contribution presents a Newtonian behavior and the polymeric stress includes the memory effects, hence,

$$\boldsymbol{\tau}^s = 2\mu_s \mathbf{D}, \quad (4)$$

where μ_s is the solvent viscosity and $\mathbf{D} = \frac{1}{2}[\nabla \mathbf{u} + (\nabla \mathbf{u})^T]$ is the strain rate tensor. The polymeric stress $\boldsymbol{\tau}^p$ includes the elasto-viscoplastic contribution, emerging from the microstructures. For viscoelastic fluids, it is common to model the contribution of the polymeric stress as $\boldsymbol{\tau}^p = \frac{\mu_p}{\lambda} f(\mathbf{A})$, where λ is the relaxation time, μ_p is the plastic viscosity, and $f(\mathbf{A})$ is a strain function of the conformation tensor \mathbf{A} [46–48]. We assume $f(\mathbf{A}) = (\mathbf{A} - \mathbf{I})$ and \mathbf{A} follows a linear relaxation law $\overset{\nabla}{\mathbf{A}} = -\frac{1}{\lambda}(\mathbf{A} - \mathbf{I})$, where $\overset{\nabla}{(\cdot)}$ is the upper-convected time derivative. Adding a critical yield stress at which the material switches between liquid and solid phase, we arrive at a constitutive law, first formulated by Saramito [26,27]. The model combines the Bingham (viscoplastic)

[49,50] and the upper-convected Maxwell (viscoelastic) models [46–48,51,52]. The polymeric stress then is governed by

$$\lambda \overset{\nabla}{\boldsymbol{\tau}}^p + \max\left(0, 1 - \frac{\tau_0}{\|\boldsymbol{\tau}^p\|}\right) \boldsymbol{\tau}^p = 2\mu_p \mathbf{D}, \quad (5)$$

where τ_0 is the yield stress, $\|\boldsymbol{\tau}^p\| = \sqrt{\text{tr}(\boldsymbol{\tau}^p{}^2)}$, and $\overset{\nabla}{\boldsymbol{\tau}}^p$ is given by

$$\overset{\nabla}{\boldsymbol{\tau}}^p = \frac{\partial \boldsymbol{\tau}^p}{\partial t} + (\mathbf{u} \cdot \nabla) \boldsymbol{\tau}^p - (\nabla \mathbf{u}) \boldsymbol{\tau}^p - \boldsymbol{\tau}^p (\nabla \mathbf{u})^T. \quad (6)$$

A dimensionless version of these equations can be obtained by scaling the variables as follows:

$$\begin{aligned} \mathbf{x} &= \mathcal{L} \bar{\mathbf{x}}, \quad t = \frac{\mathcal{L}}{U} \bar{t}, \quad \mathbf{u} = U \bar{\mathbf{u}}, \\ p &= \rho_d U^2 \bar{p}, \\ \boldsymbol{\tau}^p &= \rho_d U^2 \bar{\boldsymbol{\tau}}^p, \end{aligned} \quad (7)$$

where \mathbf{x} is the position vector, t is time, $U = \sqrt{\frac{\sigma}{\rho_d \mathcal{L}}}$ is the characteristic velocity, ρ_d is the droplet density, and the length scale is $\mathcal{L} = [3\mathcal{V}/(4\pi)]^{1/3}$ with \mathcal{V} being the volume of the droplet (\mathcal{L} can be seen as the radius of a corresponding spherical droplet with same volume \mathcal{V}).

Removing, for convenience, the bars in (7), the dimensionless governing equations for the droplet phase are given by

$$\nabla \cdot \mathbf{u} = 0, \quad (8)$$

$$\begin{aligned} \frac{\partial \mathbf{u}}{\partial t} + \nabla \cdot (\mathbf{u}\mathbf{u}) &= -\nabla p + \nabla \cdot (2 Oh_s \mathbf{D}) + \nabla \cdot \boldsymbol{\tau}^p + Bo \cdot \mathbf{g} \\ &+ \kappa \delta_s \mathbf{n}, \end{aligned} \quad (9)$$

$$De \overset{\nabla}{\boldsymbol{\tau}}^p + \max\left(0, 1 - \frac{\mathcal{J}}{\|\boldsymbol{\tau}^p\|}\right) \boldsymbol{\tau}^p = 2 Oh_p \mathbf{D}, \quad (10)$$

with the dimensionless groups: Ohnesorge numbers (Oh_s and Oh_p), Bond number (Bo), plastocapillary number (\mathcal{J}), and Deborah number (De) defined, respectively, as

$$\begin{aligned} Oh_s &= \frac{\mu_s}{\sqrt{\rho_d \sigma \mathcal{L}}}, \quad Oh_p = \frac{\mu_p}{\sqrt{\rho_d \sigma \mathcal{L}}}, \quad Bo = \frac{\rho_d g \mathcal{L}^2}{\sigma}, \\ \mathcal{J} &= \frac{\tau_0 \mathcal{L}}{\sigma}, \quad De = \lambda \sqrt{\frac{\sigma}{\rho_d \mathcal{L}^3}}. \end{aligned} \quad (11)$$

The Ohnesorge numbers compare the characteristic Rayleigh timescale and the viscocapillary time scale and, for this problem, could be seen as normalized solvent or polymeric viscosities. The Bond number compares the gravitational stresses and capillary pressure. In the present study, we focus on pure capillary spreading, where gravity is negligible, hence $Bo = 0$ in all simulations. Although we admit that the limit of large Bo and negligible surface tension is interesting and important for geophysical problems like lava flows, mudslides, and snow avalanches where large-scale EVP fluids flow under gravity [53,54]. The plastocapillary number compares the yield stress and the capillary stresses, and the Deborah number is the ratio of the polymeric relaxation time to the characteristic time scale of the problem. Note that many authors choose to replace parameters Oh_s and Oh_p by $Oh = Oh_s + Oh_p$ and

$\beta = Oh_s/(Oh_s + Oh_p)$ [55], where β can be seen as the normalized ratio of solvent to apparent viscosity. We also note that, using the present multiphase method, we also have fluid motion in the air phase. Therefore, a set of equations similar to Eqs. (8)–(10), but with Newtonian rheology, is also solved for the air flow. Consequently, two other nondimensional parameters are also relevant: the density ratio between droplet and air (ρ_d/ρ_a) and viscosity ratio (μ_s/μ_a), where subscript a denotes air properties. Both of these ratios are kept constant with a value of 100.

Limits of Eqs. (8)–(10) for the capillary flows worth mentioning:

Case 1: $\mathcal{J} = 0$ — Visco-elastocapillarity regime.

Omitting the yield stress leads to a purely viscoelastic (Oldroyd-B) fluid under capillary forces [56–60].

Case 2: $De = 0$ — Plastocapillarity regime.

Excluding viscoelastic (memory) effects results in a purely viscoplastic (Bingham) free surface flow under capillary stresses [61]. Note that, substituting $De = 0$ in Eq. (10), from Eq. (9), we arrive at the deviatoric stress of

$$\boldsymbol{\tau} = 2 \left[Oh_s + Oh_p + \frac{\mathcal{J}}{2\|\mathbf{D}\|} \right] \mathbf{D}, \quad (12)$$

for yielded regions. For a Bingham fluid, $\mathbf{D} = \mathbf{0}$ when the material is unyielded. Hence, numerical regularization is required. In practice, for this limit, instead of the EVP constitutive model, we will solve a regularized version of the generalized Newtonian model above [44,62].

Case 3: $\mathcal{J} = 0$ and $De = 0$ — Newtonian regime I.

Without elastoplastic rheology, we simply have a Newtonian fluid spreading due to surface tension, and the deviatoric stress tensor is

$$\boldsymbol{\tau} = 2 (Oh_s + Oh_p) \mathbf{D}. \quad (13)$$

Case 4: $De \rightarrow \infty$ — Newtonian regime II

For finite Oh_p and \mathcal{J} , if $De \rightarrow \infty$, we arrive at $\boldsymbol{\tau}^p \rightarrow \mathbf{0}$ and $\overset{\nabla}{\boldsymbol{\tau}}^p \rightarrow \mathbf{0}$. Given the finite deformation, we will have another Newtonian spreading with

$$\boldsymbol{\tau} \approx 2 Oh_s \mathbf{D}. \quad (14)$$

In other words, the polymers behave like passive scalars and do not contribute to the dynamics of the problem. This regime might not be physical because, in reality, the viscous and plastic dissipations might also depend on the relaxation time. Note, if Oh_p/De (\sim elastic module) remained finite, then equation (10) converged to the constitutive model of an elastic solid [48].

Case 5: $\mathcal{J} \rightarrow \infty$ — Elastocapillarity regime.

For a finite De , when the plastocapillary number is large, Eq. (10) reduces to

$$\overset{\nabla}{\boldsymbol{\tau}}^p = 2 \frac{Oh_p}{De} \mathbf{D}, \quad (15)$$

i.e., the stress inside the material remains below the yield stress and the polymeric response is elastic. In fact, $Oh_p/De = \mu_p \mathcal{L}/\sigma \lambda$ is the elastocapillary number (or the inverse of it [56]). In this limit, the droplet behaves like a Kelvin-Voigt solid that spreads under capillary stress [63–65]. This regime

is highly related to other soft wetting phenomena, where capillarity forces deform soft solids [66–68].

In all of the cases above, the system of equations is closed with appropriate boundary conditions. We apply a no-slip condition on the solid wall. Rotational symmetry is applied at the center of the droplet and outflow boundary conditions are used at the two boundaries distant from the droplet.

C. Initial condition and numerical method

We used the open source code Basilisk C to solve the equations described in the previous section. An overview of the numerical procedure will be given in this section. Detailed descriptions of Basilisk can be found in [69] (also see Appendices A 1 and A 2).

The simulation is setup by initializing a droplet according to the following shape:

$$h(r, 0) = h_\infty + R_0 \max(0, 1 - (r/R_0)^2), \quad \text{with} \\ R_0 = 1, \quad (16)$$

which represents a half-parabola in an axisymmetric coordinate system. The droplet is placed in a squared domain with dimensions $[0, 5R_0] \times [0, 5R_0]$, which is fully discretized with a nonuniform quadtree grid [70,71]. To accurately resolve the flow structure inside the droplet and its shape, we apply increased refinement levels for the liquid phase and also at the interface (see Appendix A 1). As the droplet spreads over time, the mesh is also adapted so that the refined region follows the interface.

The interface is represented implicitly by the volume-of-fluid (VOF) scheme [72], in which each mesh cell stores a value representing the fraction of droplet fluid. Density and viscosity are then locally determined based on the volume fraction $c(\mathbf{x}, t)$ according to

$$\rho(c) = c \rho_d + (1 - c)\rho_a, \quad (17)$$

$$\mu(c) = c \mu_d + (1 - c)\mu_a, \quad (18)$$

where ρ and μ represent the density and dynamic viscosity of a fluid, respectively. The subscripts d and a represent the droplet and the air, respectively.

This volume fraction field c is then advected over time by solving the equation

$$\frac{\partial c}{\partial t} + \nabla \cdot (c\mathbf{u}) = 0. \quad (19)$$

The numerical code then solves the governing equations using a projection method and a multilevel Poisson solver (see [71,73] for more details of the VOF implementation and Appendix A 3 for the present code and validation tests).

III. RESULTS AND DISCUSSION

We construct the discussion on EVP spreading by first analyzing the results of pure viscoplastic and viscoelastic droplets. In all simulations in this section, the following parameters are fixed: $Oh_s = 1/90$, $Oh_p = 8/90$, $Bo = 0$.

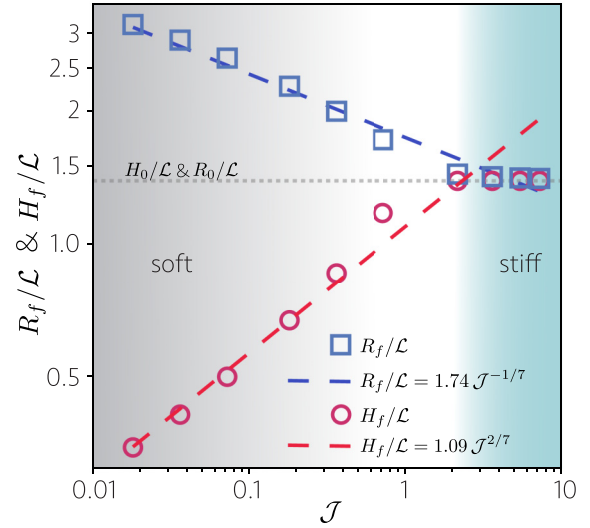


FIG. 2. Droplet final radius and height as a function of the plastocapillary number. Symbols are the present numerical simulations. The thick dashed lines show the theoretical predictions from [44]. The gray horizontal line indicates the initial radius and height of the droplets.

A. Plastocapillarity

Theoretical, computational, and experimental results for viscoplastic droplet spreading ($De = 0$) have been previously presented [25,44]. We will revisit this limit first to validate the simulation and also to extend the available results for higher plastocapillary numbers. To this end, we will focus on the properties of the final shape of the droplet when $t \rightarrow \infty$. Unlike Newtonian droplets, droplets of yield-stress fluids will be arrested at this limit, resulting in a finite final radius R_f and height H_f . In a pure viscoplastic case, these features can be explained by balancing the capillary stress and yield stress [44], resulting in theoretical scaling laws, $R_f/L = 1.74 J^{-1/7}$, $H_f/L = 1.09 J^{2/7}$. Note, the prefactors are obtained from asymptotic analysis [44]. Also note, to test our numerical results against these laws, we must choose a stoppage criterion in our simulations since we used a regularized model in the viscoplastic limit. We do this based on the nondimensional kinetic energy $[E_k = (1/\sigma L^2) \int_V \frac{1}{2} \rho_d \|\mathbf{u}\|^2 dV]$ of the droplet, such that the simulation is stopped when $E_k < 10^{-6}$.

Figure 2 shows the final radius and height of our simulated droplets versus the plastocapillary number J . As expected, due to the higher influence of yield stress on capillary-driven spreading, the final radius decreases with J , while the final height increases. Both final radius and height reach a plateau after a certain value of plastocapillary number, $J \approx 1$ (see Video I within the Supplemental Material [74]). At this limit, the droplets practically get stuck at their initial shape, since the capillary stress is not strong enough to overcome the yield stress at all. There exists a transition regime between the low yield-stress scaling laws (soft) and the high yield-stress plateau (stiff) regimes, where the numerical results smoothly vary between the two. There is a good agreement between the theory and numerical results when the droplets are soft enough to yield. As plastocapillary number increases, the droplet does

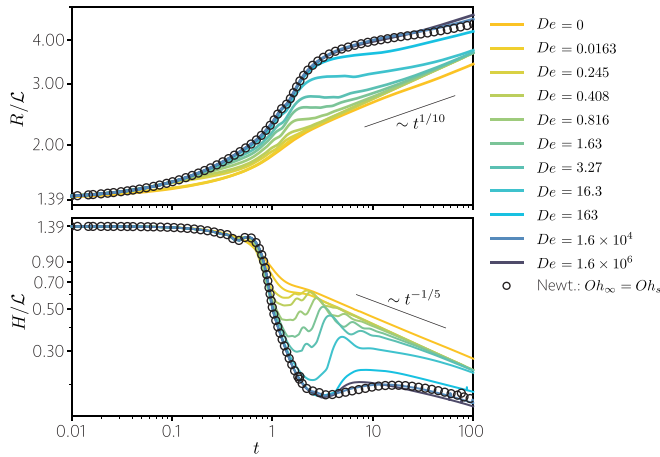


FIG. 3. Spreading radius (top) and height (bottom) over time for different values of the Deborah number.

not entirely yield and hence breaks the assumption in the theoretical predictions. Note that the exact point of transition from soft to stiff limit depends on the initial conditions. This could have important implications for some applications such as 3D printing [25,75–79], when depending on the values of \mathcal{J} , the history (shape) of droplet/filament at the time of deposition can influence the final geometry of the print.

B. Visco-elastocapillarity

We continue by considering the case of viscoelastic materials without plasticity, that is, $\mathcal{J} = 0$. In this situation, the constitutive model reduces to an Oldroyd-B fluid. Figure 3 shows the droplet radius (top) and height (bottom) over time for different values of De (see Video II within the Supplemental Material [74]). In the Newtonian limit ($De = 0$), the spreading eventually follows the rate predicted by Tanner’s law [7], i.e., $R \propto t^{1/10}$ and $H \propto t^{-1/5}$. For the viscoelastic case, we note that, in the first moments, the droplet spreads considerably more as we increase De . We anticipate this is due to the increased relaxation time of the fluid. As we increase the relaxation time (or De), the stresses take a longer time to develop as the flow field develops inside the droplet, consequently, the droplet spreads more since the internal stress is smaller during this transient period. As a consequence, interestingly, the spreading curves converge to an apparent Newtonian limit when $De \rightarrow \infty$. In this limit, the polymeric stress does not have enough time to develop at all within the timescale of the simulation, and we actually recover a Newtonian droplet that only exhibits the solvent stress, i.e., we have a Newtonian fluid with Ohnesorge number $Oh_\infty = Oh_s$ (circles in Fig. 3). For the intermediate values of De , the interface experiences an oscillatory behavior (see Fig. 3), where the droplet height first reaches a local minimum and then increases again as elastic stresses build up, eventually reaching a decaying regime.

To further analyze the anatomy of viscoelastic spreading, we inspect the flow field inside the droplet using a flow parameter [80],

$$\xi = \frac{|\mathbf{D}| - |\mathbf{\Omega}|}{|\mathbf{D}| + |\mathbf{\Omega}|}, \quad (20)$$

where \mathbf{D} and $\mathbf{\Omega}$ are the deformation rate and vorticity tensors (the symmetric and antisymmetric components of $\nabla\mathbf{u}$), respectively: $\mathbf{D} = 1/2 [\nabla\mathbf{u} + (\nabla\mathbf{u})^T]$ and $\mathbf{\Omega} = 1/2[\nabla\mathbf{u} - (\nabla\mathbf{u})^T]$. The flow parameter can vary in the range $\xi \in [-1, 1]$, where $\xi = 1$ represents a purely extensional flow, $\xi = 0$ shear flow and $\xi = -1$ indicates solid-like rotation. Figure 4 shows the value of ξ inside a viscoelastic droplet with $De = 0.245$ for different time frames. At the beginning of spreading, the flow close to the axi-symmetry axis and in the bulk of the droplet is predominantly extensional (red color). Meanwhile, a shear-dominant boundary layer forms from the contact line and across the substrate [zone I Fig. 4(a)]. Two rotating regions also develop close to the interface and grow over time [zones II and III in Fig. 4(b)] but decay as the droplet further spreads. Eventually, the flow inside the droplet is mainly extensional in the center [zone IV in Fig. 4(d)] and shear dominant close to the substrate.

In the next step, we will study the additional effects of plasticity on the complex flow structures shown above in an EVP spreading.

C. Elasto-viscoplastic spreading

We now consider the general scenario of elasto-viscoplastic spreading, i.e., De and \mathcal{J} are both finite. In this case, all the nonlinear properties mentioned earlier (including the coexistence of solid and liquid states in plastic fluids and the time-dependent characteristics of viscoelastic fluids) are simultaneously observed. We inspect the nondimensional polymeric stress τ^p and observe in which regions this stress is above (yielded) or below (unyielded) the value of \mathcal{J} (see [43]). Figure 5 shows the value of scalar $S = \log(\|\tau^p\|) - \log(\mathcal{J})$ at different times inside a droplet with $\mathcal{J} = 0.18$ and $De = 0.816$. $S > 0$ means the material is fluidized and flows like a viscoelastic fluid, and $S < 0$ means the material is not yielded and behaves like a viscoelastic solid. As expected, the droplet is initially mostly unyielded (large blue region) since we assume there is no internal stress as our initial condition. The stress begins to increase from the contact line, which is the location of the highest curvature [zone I in Fig. 5(a)]. After some time, most of the droplet is yielded (red colors) with a particularly higher stress region near the wall and droplet edge [zone II in Fig. 5(b)]. Meanwhile, a moving plug forms near the interface of the droplet [zone III in Fig. 5(b)], correlated with the rotating regions shown in Fig. 4. As time continues to increase, the droplet solidifies once again with a static plug in the center [zone IV in Fig. 5(c)], leading to a full stoppage. Note that, unlike the pure viscoplastic case, no regularization is needed in the case of EVP materials; the viscoelastic solid will reach an equilibrium state as long as stress everywhere inside the droplet is below the yield stress.

We systematically extended the analysis above by changing the control nondimensional parameters. Figure 6 demonstrates the value of S for different combinations of \mathcal{J} and De (see Video III within the Supplemental Material [74]). For a given De , increasing the value of \mathcal{J} leads to larger unyielded regions inside the droplet, which is expected as we increase the material yield-stress. Hence, for a given De , and at a given time, the droplet spreads less as the values of \mathcal{J} increase.

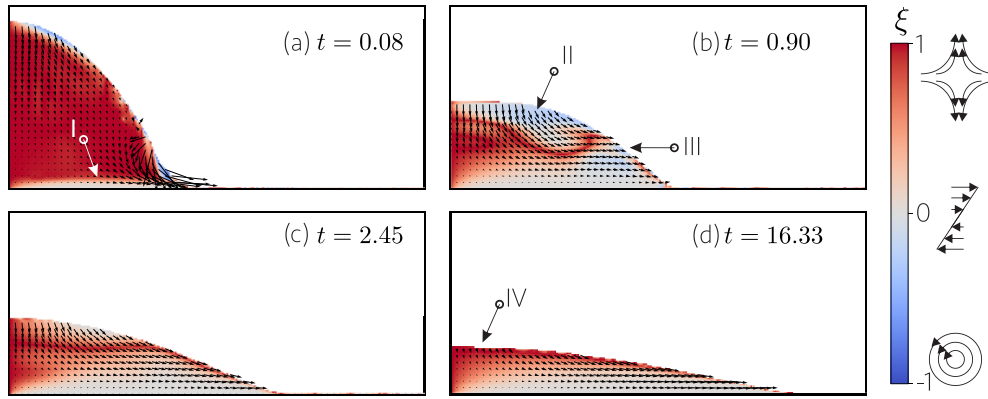


FIG. 4. Flow structure inside a viscoelastic droplet with $De = 0.245$ at different time stamps. Regions of $\xi = 0$ indicate purely shear flow, $\xi = 1$ extensional flow, and $\xi = -1$ rotation.

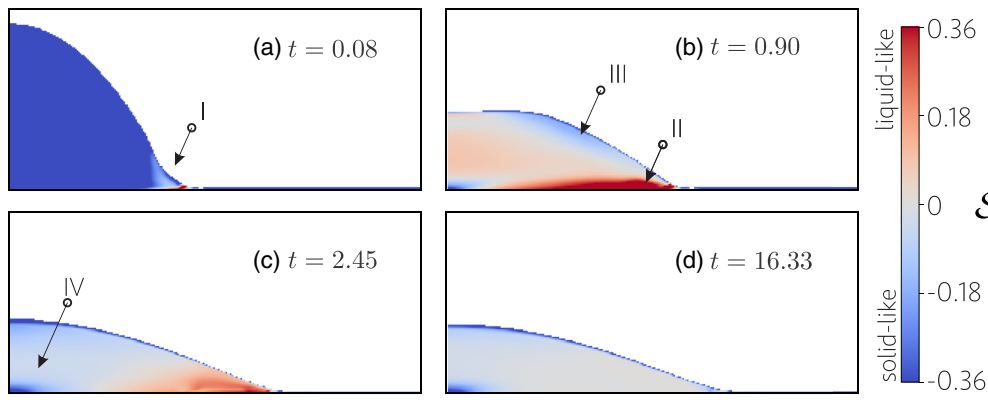


FIG. 5. Distribution of S at different timestamps inside an elasto-viscoplastic droplet with $De = 0.816$ and $\mathcal{J} = 0.18$. Blue regions indicate stress below the plastocapillary number \mathcal{J} (unyielded) and red regions are above \mathcal{J} (yielded).

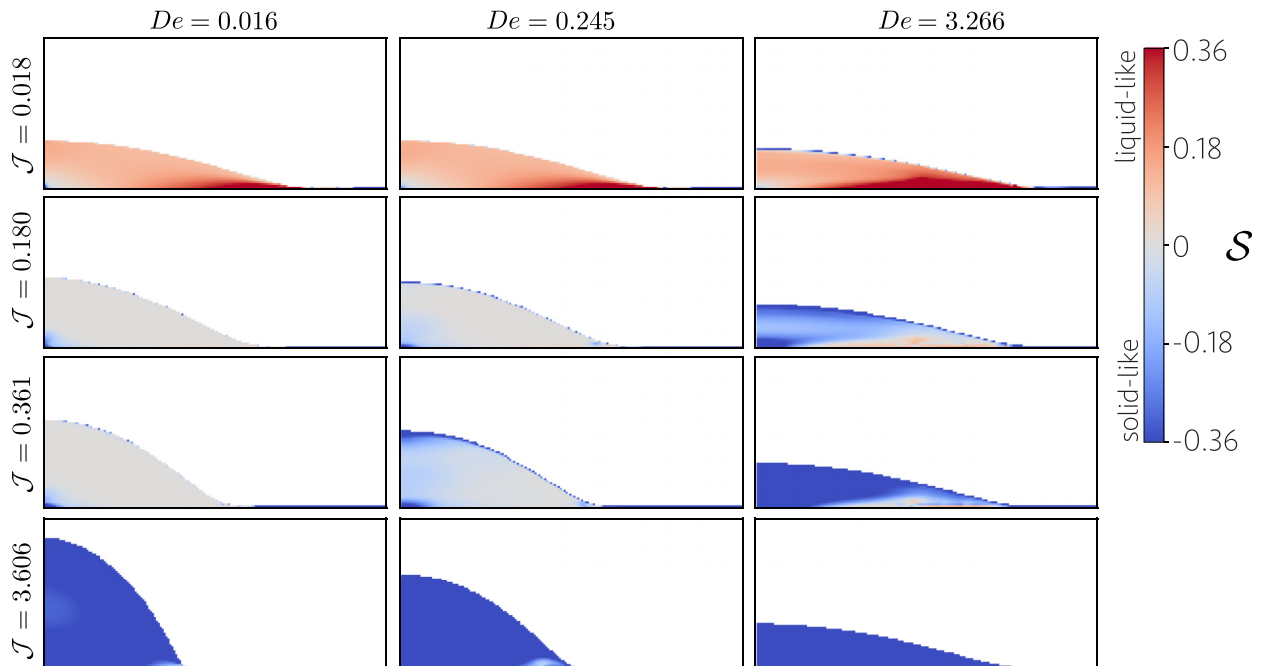


FIG. 6. Distribution of S inside the elasto-viscoplastic droplet for different values of De and \mathcal{J} . All snapshots are taken at time $t = 8.16$ (see Video III within the Supplemental Material [74]). Blue regions indicate stress below the plastocapillary number \mathcal{J} (unyielded) and red regions are above \mathcal{J} (yielded). We note that the colorbar limits do not include the total range of values present in the data, since we are only interested in visualizing regions that are above or below zero.

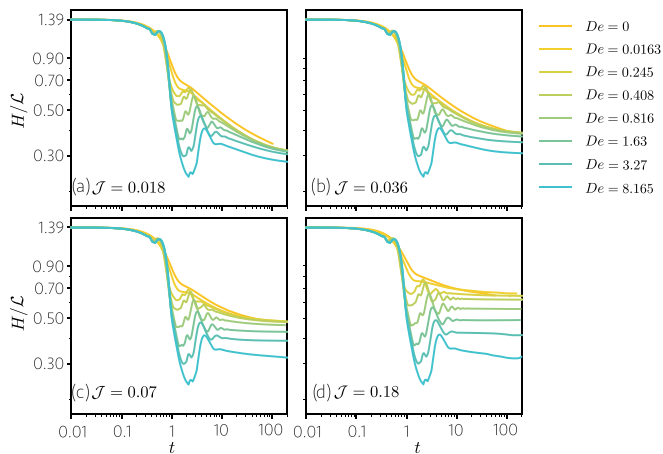


FIG. 7. The evolution of droplet height as a function of the plastocapillary and Deborah numbers.

For a given \mathcal{J} , increasing the Deborah number also generates larger unyielded regions (in blue). Similarly to the explanation in Sec. III B, increasing De results in smaller values of τ^p and more regions below the yield stress. Intriguingly, at the high \mathcal{J} cases (last row in Fig. 6), it is notable to observe that by increasing De , the droplet spreads significantly even though it almost entirely behaves like a solid. This is because the current EVP formulation models the unyielded case as a viscoelastic solid, allowing for a finite deformation rate (as opposed to a Bingham rigid solid where the deformation rate is zero for the solid state). This means that the material can experience deformation even below the yield stress, as seen clearly in the examples when both \mathcal{J} and De are high (elastocapillarity regime).

For a better quantitative analysis of the dynamics shown above, we look at the variation of droplet height over time for different values of \mathcal{J} and De , as shown in Fig. 7. For EVP droplets the spreading stops and a final shape is reached. This is similar to the plastocapillarity regime; however, the elasticity clearly influences the final shape. Similarities to the visco-elastocapillarity regime can also be seen, particularly in the local overshoot and the oscillation of the height that is observed for most cases and amplifies with De . At the same time, the impact of De on the dynamics is more pronounced for higher values of \mathcal{J} , resulting in a larger difference in the final shape (height and radius).

Finally, we quantify the Deborah number effects on the final radius of the droplet to complete the picture shown in Sec. III A. Figure 8 shows the final radius of droplet versus \mathcal{J} for different values of De . The limit $De = 0$ corresponds to a viscoplastic limit, also shown in Fig. 2 and the dashed lines represent the theoretical scaling for this case. As De increases, the droplet spreads more, particularly for higher values of \mathcal{J} . For higher De values, we also see a decrease in the critical value of \mathcal{J} from which the spreading stays almost constant. This happens because, as we saw earlier, the elasticity promotes unyielded droplets, and for droplets that are already unyielded, further increasing the value of \mathcal{J} does not introduce further changes. For the elastocapillarity limit, when De and \mathcal{J} are large, balancing the surface tension and

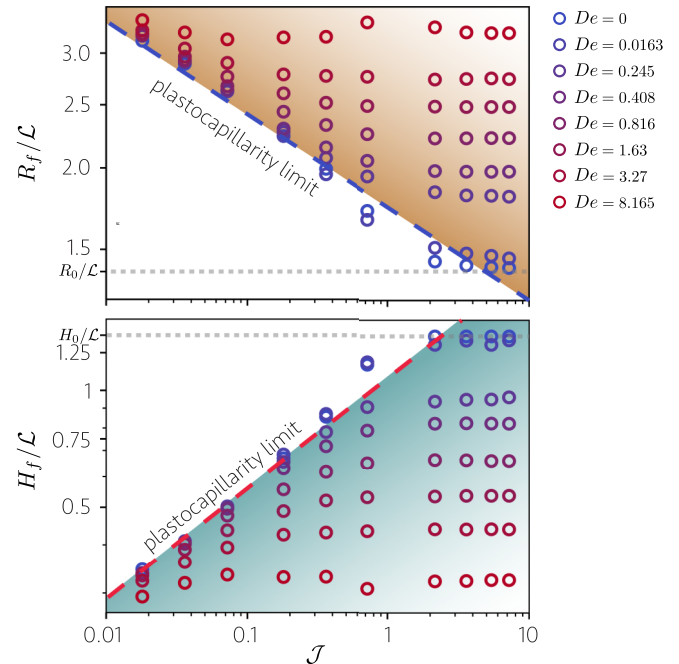


FIG. 8. Final radius (top) and height (bottom) of EVP droplets for a range of \mathcal{J} and De . The horizontal dashed gray lines show the initial radius and height. The thick blue and red dashed lines correspond to the plastocapillarity limits (see Sec. III A).

elastic forces results in scaling laws for the final radius and height of the droplet. At the stoppage moment, the surface tension force can be estimated as $F_\sigma = \sigma \mathcal{H}_f^2 / \mathcal{R}_f$. Balancing this with the elastic forces, estimated as $F_e = (\mu_p / \lambda) \mathcal{R}_f^2$, and a for a given volume of the droplet $\mathcal{V} \sim \mathcal{L}^3 \sim \mathcal{H}_f \mathcal{R}_f^2$, we arrive at $\mathcal{R}_f / \mathcal{L} \sim (Oh_p / De)^{-1/7}$ and $\mathcal{H}_f / \mathcal{L} \sim (Oh_p / De)^{2/7}$. These formulations are similar to those for the plastocapillarity limit, except that the plastocapillary number (yield stress) is replaced by elastocapillary number (elastic modulus). In Appendix A 4, we test these scaling laws by looking at the final radius and height as a function of De .

IV. CONCLUSIONS

We numerically investigated the spreading of elasto-viscoplastic fluids under surface tension forces. Direct numerical simulations are performed using the EVP model of Saramito to understand how different nondimensional groups influence the spreading. We focused our study on the importance of two nondimensional groups: the plastocapillary number \mathcal{J} , and the Deborah number De . We confirm that increasing the plastocapillary number in EVP spreading, reduces the droplet spreading, as previously explained for the viscoplastic limit [25,44]. The influence of elasticity on spreading can also be significant. Increasing the Deborah number (while other parameters are fixed) promotes more spreading. This effect is associated with the polymeric relaxation time, which delays the development of the internal droplet stresses, allowing the droplet to spread with less resistance.

Overall, for fixed (solvent and polymeric) Ohnesorge numbers, the $De - \mathcal{J}$ parameter space covers a range of regimes,

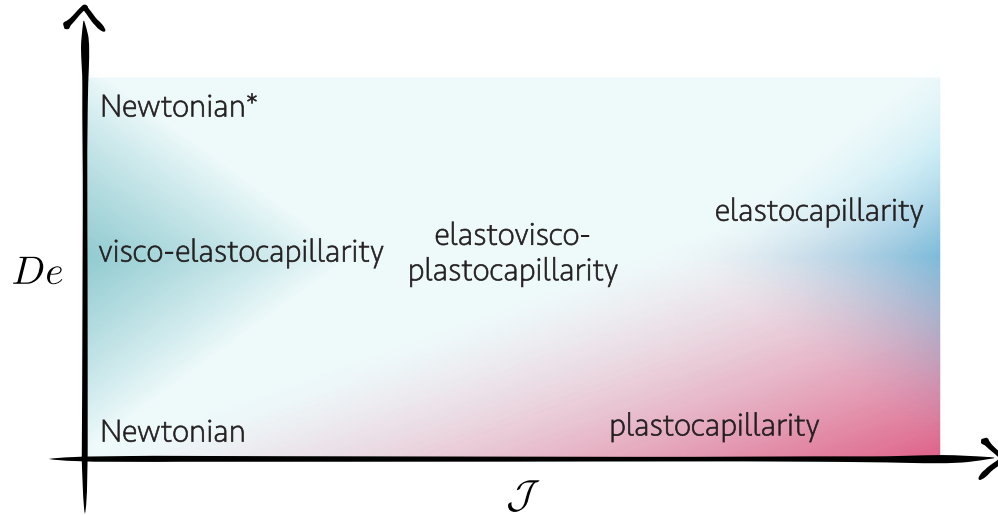


FIG. 9. $De - \mathcal{J}$ parameter space and its different limits. The general case of EVP spreading reaches different regimes, depending on which rheological factor (elasticity or plasticity) dominates. Note that the high De regime of Newtonian fluids is for finite Oh_p .

including visco-elastocapillarity, elastocapillarity, and plastocapillarity, which can be further studied by the model presented here. Figure 9 presents a (schematic) overview of these limits.

The spreading of EVP fluids plays a key role in many industrial applications, such as coating and 3D printing. Our paper, based on a continuum model, sheds light on how elastic and plastic rheological properties alter viscous spreading. The study can be further extended in many different ways. Firstly, further experimental studies are required. The present experimental data [44] are limited to viscoplastic limits and are not sufficient to compare with the simulations here. Ideally, experiments in which the values of plastocapillary and the Deborah numbers can be systematically changed should be performed. This, however, could be a difficult task as chemical or physical changes in microstructure often change the yield stress, viscosity, and elastic moduli of the material, simultaneously. The EVP model of Saramito, used here, is relatively simple to implement and describes a large number of physical phenomena at various limits. However, the model does not consider transient yielding and predicts a linear elastic solid response for small strains (see Fig. 16 below), which does not hold for most elasto-viscoplastic materials. Including other mechanisms, like kinematic hardening [29,81], accounts for a more realistic transient yielding processes. More recently, Kamani *et al.* [82,83] presented a model that features a rate-dependent relaxation time, allowing for plastic deformation when stress is below the yield stress. The model nicely presents the transient yielding, which might affect dynamical processes like droplet spreading. Hence, one improvement of the present results could be the implementation of such models. We aim to address this in our future work.

The present article focuses on the problem of spreading. Still, in principle, the computational framework presented here could be used to study and analyze a range of capillary-driven phenomena such as bubble or drop coalescence [84–88], pinch-off [89,90], multicomponent systems like drops on liquid-infused surfaces [91,92] or soft wetting [66,68,93,94], and nonaxisymmetric shapes [76]. The model

can also be used to study the complex flow history effects, such as the effect of nozzle flow on the final deposition of 3D printers. Finally, the model can be extended for materials with more complicated rheological properties such as thixotropy [20,95,96] and also for wetting of dry surfaces, when a triple line exists [23].

ACKNOWLEDGMENTS

The authors would like to thank D. Bonn, T. Appleford, A. Gaillard, E. Chaparian, and V. Sanjay for insightful discussions. We also thank the financial support given by Sao Paulo Research Foundation (FAPESP) Grants No. 2013/07375-0, No. 2019/01811-9, and No. 2021/14953-6, and the National Council for Scientific and Technological Development (CNPq), Grant No. 305383/2019-1.

APPENDIX: NUMERICAL REGULARIZATION AND GRID DEPENDENCY

1. Viscoplasticity and viscoelasticity

We use a generalized Newtonian Bingham model when $De = 0$, i.e., a viscoplastic material. In this case, the apparent viscosity is replaced by a regularized Bingham-Papanastasiou viscosity [97]

$$\mu_{\text{app}} = Oh_s + Oh_p + \frac{\mathcal{J}}{2\|\mathbf{D}\|} (1 - e^{-\|\mathbf{D}\|/\epsilon_{vp}}), \quad (\text{A1})$$

where ϵ_{vp} is the regularization parameter (see [98]). Figure 10 shows an example of convergence tests for the viscoplastic regularization parameter when $\mathcal{J} = 0.18$, $Oh_s + Oh_p = 0.1$, $De = 0$, $Bo = 0$ and the interface is captured at time $t = 10$. Performing a series of these tests, we note that all solutions have converged for values $\epsilon_{vp} \leq 10^{-3}$. Therefore, in all viscoplastic simulations reported in this article, we fixed $\epsilon_{vp} = 10^{-3}$.

An adaptive quadtree mesh is used in all the simulations in this paper. An example of nonuniform grids is shown in Fig. 11. The maximum level of refinement is initially applied

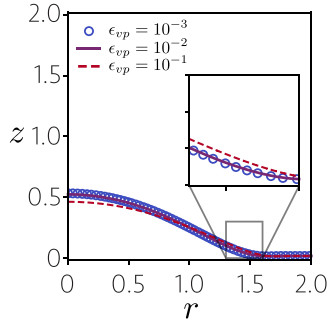


FIG. 10. Convergence tests for the Bingham regularization parameter. The plastocapillary number is $\mathcal{J} = 0.18$ and the mesh is fixed at Level = 10.

only near the interface, while one level coarser is used everywhere inside the droplet. Over time, the adaptive mesh refinement may also impose the maximum level in regions inside the droplet, based on error estimations on the velocity and volume fractions. In the outer (air) phase, the size of the grids gradually increases from the interface. We checked for the effect of grid size on the numerical results presented here to ensure the reported outcomes on dynamics of spreading and the droplet shapes are independent of the grid size. In Fig. 12(a), the maximum mesh refinement level is varied for a fixed $\epsilon_{vp} = 10^{-3}$. The change in the interface dynamics is negligible when Level ≥ 10 . With these results in mind, all the viscoplastic simulations in this paper are performed with $\epsilon_{vp} = 10^{-3}$ and Level = 10.

We now perform a convergence test for the case of viscoelastic droplets ($\mathcal{J} = 0$ and $De \neq 0$). In this situation, no viscoplastic regularization needs to be used, so we only check for mesh convergence. Figures 12(b) and 12(c) show the radius and height of the droplet over time for different mesh levels with fixed $De = 0.41$. We note that little difference is observed with mesh levels above 9. For this reason, all the viscoelastic simulations performed in this work will use the mesh level 10.

2. Elasto-viscoplasticity

When $De \neq 0$ and $\mathcal{J} \neq 0$, the full Saramito constitutive equations (10) are used. The software Basilisk already con-

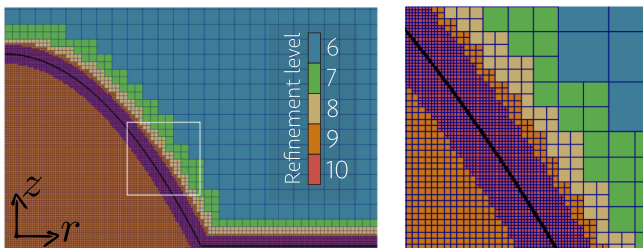


FIG. 11. Nonuniform grid generated for the spreading simulation. The right panel shows the magnified view of the white box in the left. Cells are colored by their level of refinement (the computational domain is a square and has a level 0 refinement; see [70]). We note that this figure does not capture the entire domain, which continues both in the r and z directions.

tains a well-tested implementation of the Oldroyd-B model for solving viscoelastic flows given the parameters λ (relaxation time) and μ_p (polymeric viscosity) [99]. To make use of this existing module, we rewrote the Saramito constitutive equation (10) as

$$\frac{De}{\alpha} \nabla \cdot \boldsymbol{\tau}^p + \boldsymbol{\tau}^p = 2 \frac{Oh_p}{\alpha} \mathbf{D}, \quad \text{where} \quad \alpha = \max \left(\epsilon_{vp}, 1 - \frac{\mathcal{J}}{\|\boldsymbol{\tau}^p\|} \right), \quad (\text{A2})$$

and ϵ_{vp} is a small threshold parameter. We note that equation (A2) has the same form as the traditional Oldroyd-B equation but with nonconstant relaxation time and polymeric viscosity coefficients. Therefore, we use the standard Oldroyd-B solver in Basilisk by dynamically setting these two coefficients according to the expressions in Eq. (A2).

Figure 13 shows convergence tests for the EVP threshold parameter and for the mesh refinement parameter in a simulation with $De = 0.816$ and $\mathcal{J} = 0.18$. We observe that ϵ_{vp} has negligible influence on the shape of the droplet, even at relatively large values. Regarding mesh convergence, we see that for refinement levels above 9, the results are already very similar. For all the following EVP simulations in this article, we used the combination $\epsilon_{vp} = 10^{-7}$ and Level = 10.

3. Appendix: Validation

We present a number of validation cases where theoretical results are available. All codes are available on GitHub [100].

a. Startup shear flow

A basic rheology test for non-Newtonian fluids is the startup shear flow between two parallel plates, which we will use here to test our code. We nondimensionalize the equations using the domain half-height H as length scale and $U = H\dot{\gamma}_{xy}$ as velocity scale, where $\dot{\gamma}_{xy}$ is the imposed shear rate. In this manner, we arrive at

$$\nabla \cdot \mathbf{u} = 0, \quad (\text{A3})$$

$$Re \left(\frac{\partial \mathbf{u}}{\partial t} + \nabla \cdot (\mathbf{u}\mathbf{u}) \right) = -\nabla p + \nabla \cdot (2\beta \mathbf{D}) + \nabla \cdot \boldsymbol{\tau}^p, \quad (\text{A4})$$

$$Wi \left(\frac{\partial \boldsymbol{\tau}^p}{\partial t} + (\mathbf{u} \cdot \nabla) \boldsymbol{\tau}^p - (\nabla \mathbf{u}) \boldsymbol{\tau}^p - \boldsymbol{\tau}^p (\nabla \mathbf{u})^T \right) + \max \left(0, 1 - \frac{Bi}{\|\boldsymbol{\tau}^p\|} \right) \boldsymbol{\tau}^p = 2(1 - \beta) \mathbf{D}, \quad (\text{A5})$$

with the dimensionless groups: Reynolds number (Re), Bingham number (Bi), Weissenberg number (Wi), and viscosity ratio ($\beta \in (0, 1)$) defined respectively as

$$Re = \frac{\rho \dot{\gamma}_{xy} H^2}{\mu_0}, \quad Bi = \frac{\tau_0}{\mu_0 \dot{\gamma}_{xy}}, \quad Wi = \lambda_p \dot{\gamma}_{xy}, \quad \beta = \frac{\mu_s}{\mu_0}, \quad (\text{A6})$$

where $\mu_0 = \mu_s + \mu_p$ is the total viscosity.

We model the geometry as a rectangular domain $[-10, 10] \times [-1, 1]$ and impose the velocity $u_x = 1$ at the top boundary and $u_x = -1$ at the bottom boundary, such that the nondimensional shear rate is $\dot{\gamma}_{xy} = 1$.

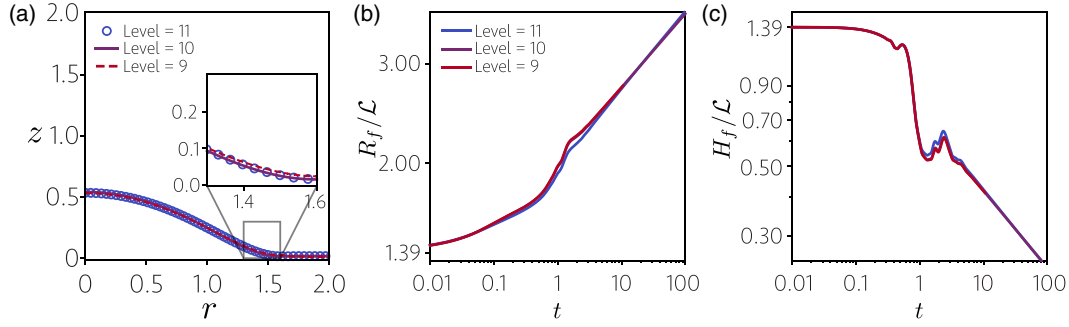


FIG. 12. Mesh convergence tests for a Bingham material and a viscoelastic fluid. (a) Snapshot of a Bingham droplet at time $t = 10$ with fixed $\epsilon_{vp} = 10^{-3}$ and $\mathcal{J} = 0.18$. [(b),(c)] Radius and height evolution for a viscoelastic droplet with $De = 0.41$ and different mesh refinements.

Figure 14 shows the values of polymeric stress components obtained for three values of Bi and five values of Wi . In the same figure, we also plot the semi-analytical solution for this problem obtained in [26]. We observe good agreement between the two solutions, which indicates that the code developed here is correctly capturing the evolution of the EVP stress over time.

b. Oscillatory shear flow

Oscillatory shear tests are also standard benchmark flows for non-Newtonian fluids. For this test, we impose a periodic deformation given by $\gamma(t) = \gamma_0 \sin(\omega t)$, where γ_0 is the strain amplitude while ω is the frequency. Consequently, the deformation rate is $\dot{\gamma}(t) = \gamma_0 \omega \cos(\omega t)$. We nondimensionalize the problem with the following rescalings:

$$\begin{aligned} \mathbf{x} &= H\bar{\mathbf{x}}, \quad t = \frac{1}{\omega}\bar{t}, \quad \mathbf{u} = \gamma_0 H \omega \bar{\mathbf{u}}, \quad p = \gamma_0 \mu_0 \omega \bar{p}, \\ \boldsymbol{\tau}^p &= \gamma_0 \mu_0 \omega \bar{\boldsymbol{\tau}}^p. \end{aligned} \quad (\text{A7})$$

With these choices, we obtain the same Eqs. (A3)–(A5), but with the following definitions for the nondimensional groups:

$$Re = \frac{\rho \omega H^2}{\mu_0}, \quad Bi = \frac{\tau_0}{\mu_0 \gamma_0 \omega}, \quad Wi = \lambda_p \omega, \quad \beta = \frac{\mu_s}{\mu_0}. \quad (\text{A8})$$

Figure 15 shows the Lissajous plots relating the shear stress to deformation and deformation rate with different values of

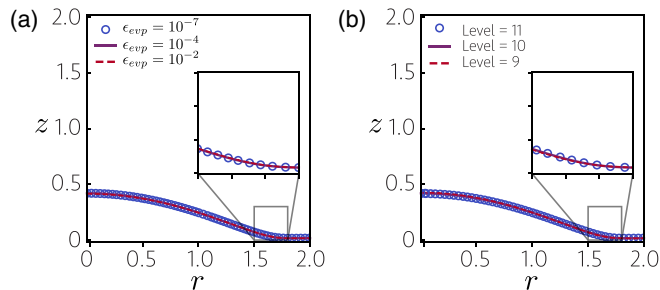


FIG. 13. Convergence tests for the EVP regularization parameter (left) and for the mesh refinement parameter (right). In the regularization tests, we keep fixed the mesh level as 10 and in the mesh tests we fix the regularization $\epsilon_{vp} = 10^{-7}$. All simulations are performed with $De = 0.816$ and $\mathcal{J} = 0.18$.

Bi and Wi . In the same figure, we also plot the semi-analytical solution for this problem obtained in [26]. Once again, good agreement is obtained, showing that the present code captures the transient dynamics of Saramito's EVP stress. Note that, in these tests, we initialize the stress with $\boldsymbol{\tau} = \mathbf{0}$, such that it requires a short amount of time before adjusting itself into its periodic cycle.

From the same tests, we can also extract the values of the storage modulus (G') and the loss modulus (G''). These are shown as circles in Fig. 16, and the straight lines represent the semi-analytical solution for a shear flow (see [26]). We note that the values of G' and G'' are given as a function of Bi^{-1} , which can be seen as a nondimensional equivalent for the strain amplitude. Also note that, as discussed in the conclusion, the Saramito model leads to the sudden drop of G'' at small strains, where only the contribution of the solvent viscosity is present.

c. Droplet under shear flow

In order to test our implementation in a problem with a moving interface, we will look into the deformation of an EVP droplet under simple shear flow in a Newtonian fluid.

We nondimensionalize the problem with the following rescalings:

$$\begin{aligned} \mathbf{x} &= R\bar{\mathbf{x}}, \quad t = \frac{1}{\dot{\gamma}_{xy}}\bar{t}, \quad \mathbf{u} = R\dot{\gamma}_{xy}\bar{\mathbf{u}}, \quad p = \mu^M \dot{\gamma}_{xy} \bar{p}, \\ \boldsymbol{\tau}^p &= \mu^M \dot{\gamma}_{xy} \bar{\boldsymbol{\tau}}^p, \quad \kappa = \frac{1}{R}\bar{\kappa}, \quad \delta_s = \frac{1}{R}\bar{\delta}_s, \end{aligned} \quad (\text{A9})$$

where R is the droplet initial radius, $\dot{\gamma}_{xy}$ is the imposed shear rate, and μ^M is the viscosity of the matrix fluid (Newtonian).

With these choices, we obtain the following nondimensional equations:

$$\nabla \cdot \mathbf{u} = 0, \quad (\text{A10})$$

$$\begin{aligned} \frac{\rho}{\mu^M} Re \left(\frac{\partial \mathbf{u}}{\partial t} + \nabla \cdot (\mathbf{u}\mathbf{u}) \right) &= -\nabla p + \nabla \cdot \left(2 \frac{\mu_0}{\mu^M} \beta \mathbf{D} \right) \\ &+ \nabla \cdot \boldsymbol{\tau}^p + \frac{1}{Ca} \bar{\kappa} \bar{\delta}_s \mathbf{n}, \end{aligned} \quad (\text{A11})$$

$$\begin{aligned} Wi \left(\frac{\partial \boldsymbol{\tau}^p}{\partial t} + (\mathbf{u} \cdot \nabla) \boldsymbol{\tau}^p - (\nabla \mathbf{u}) \boldsymbol{\tau}^p - \boldsymbol{\tau}^p (\nabla \mathbf{u})^T \right) \\ + \max \left(0, 1 - \frac{Bi}{\|\boldsymbol{\tau}^p\|} \right) \boldsymbol{\tau}^p = 2 \frac{\mu_0}{\mu^M} (1 - \beta) \mathbf{D}, \end{aligned} \quad (\text{A12})$$

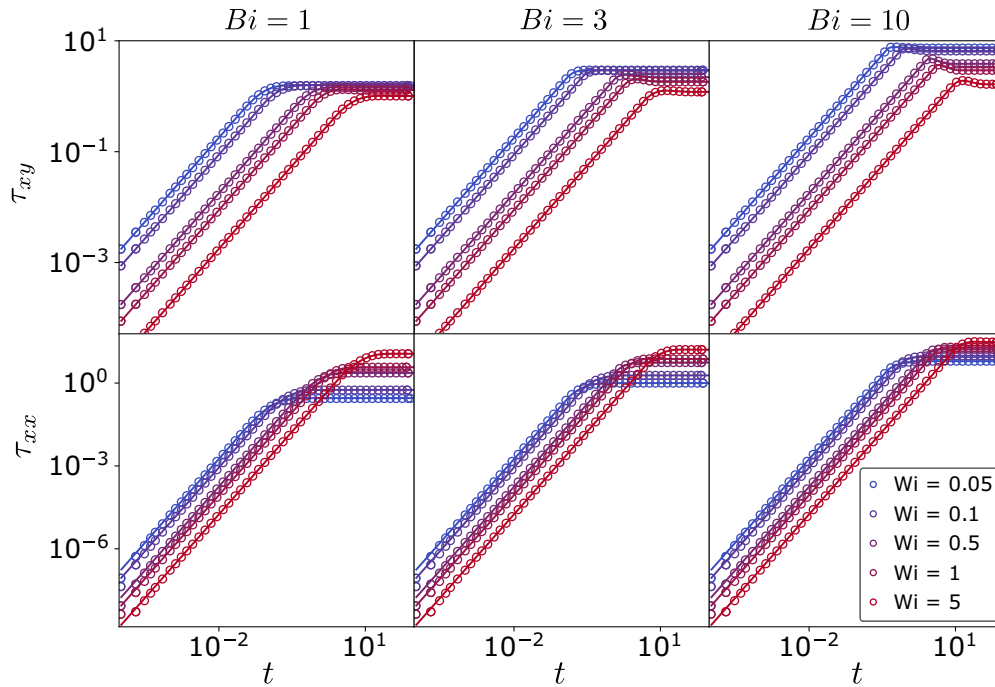


FIG. 14. Evolution of τ_{xy}^p and τ_{xx}^p over time in a start up simple shear flow. Circles correspond to the numerical solution from our code and straight lines are the semi-analytical solution to the problem (see [26]). The Reynolds number is always fixed at $Re = 0.1$ and the viscosity ratio is $\beta = 1/9$.

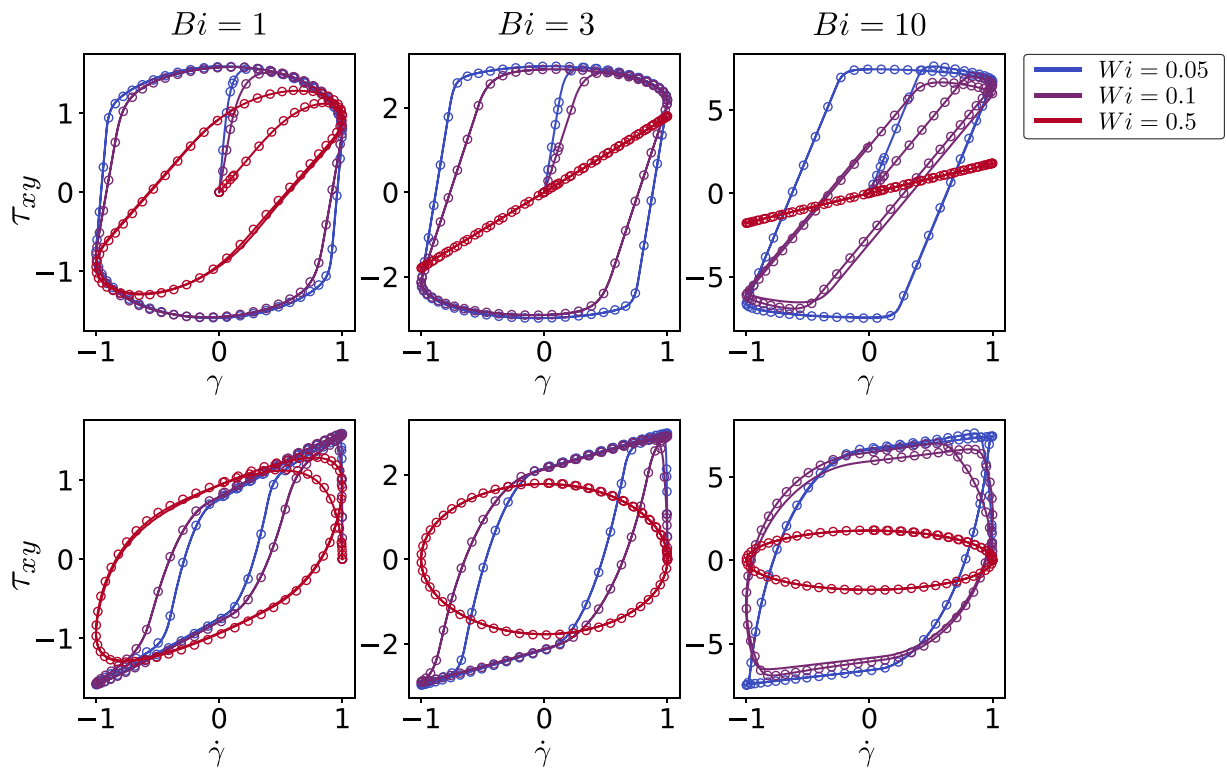


FIG. 15. Lissajous plots showing the shear stress τ_{xy}^p as a function of the periodic strain (top) and strain rate (bottom). Circles correspond to the numerical solution from our code and straight lines are the semi-analytical solution to the problem (see [26]). The Reynolds number was kept at $Re = 0.1$ and viscosity ratio at $\beta = 1/9$.

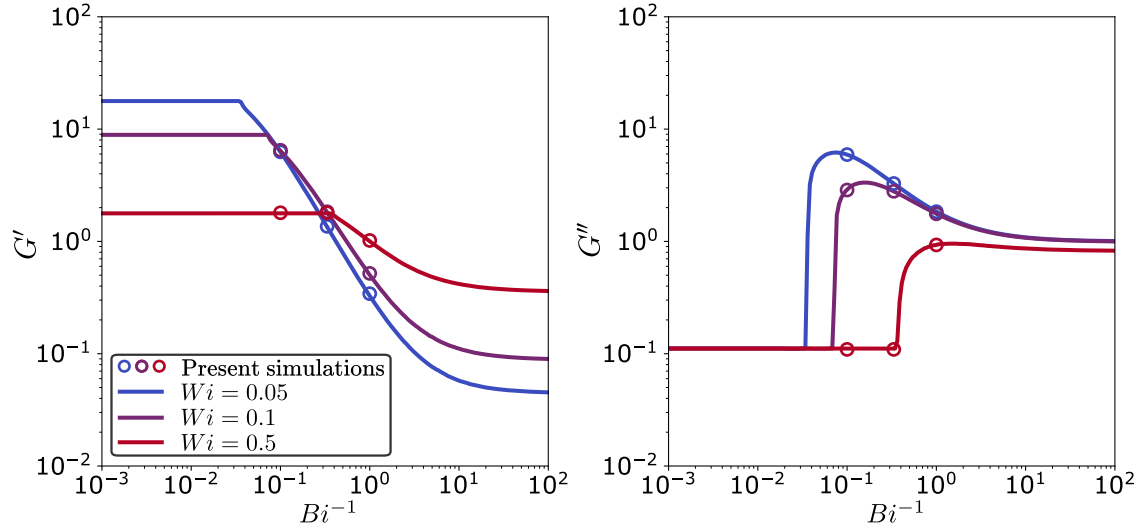


FIG. 16. Nondimensional storage (G') and loss (G'') moduli for a Saramito fluid as a function of Bi^{-1} . Circles are numerical solutions from our code corresponding to the same 9 simulations shown in Fig. 15. Straight lines are the semi-analytical solution to the problem (see [26]).

where ρ is the density of the droplet, ρ^M is the density of the fluid around it and $\mu_0 = \mu_s + \mu_p$ is the total viscosity of the droplet. The dimensionless groups are now given by

$$Re = \frac{\rho^M \dot{\gamma}_{xy} R^2}{\mu^M}, \quad Bi = \frac{\tau_0}{\mu^M \dot{\gamma}_{xy}}, \quad Wi = \lambda_p \dot{\gamma}_{xy}, \quad \beta = \frac{\mu_s}{\mu_0},$$

$$Ca = \frac{\sigma}{\mu^M \dot{\gamma}_{xy} R}. \quad (A13)$$

When subject to a constant shear flow, the circular droplet deforms into an ellipsoid shape. This can be measured by the droplet deformation parameter $D = (L - B)/(L + B)$, where L and B are lengths of the major and minor axes of the ellipse, respectively. For all tests below we will use a channel of half-height $H = 4R$, which also imposes some confinement effects on the droplet. The ratio between droplet-matrix properties will be fixed at $\frac{\mu_0}{\mu^M} = \frac{\rho}{\rho^M} = 1$.

We begin by looking into results for a Newtonian droplet ($Bi = 0, Wi = 0, \beta = 1$) as a function of the capillary number. As shown in the left panel of Fig. 17, our computational results follow the previous simulation of Zhou and Pozrikidis [101] and the (almost) linear variation, expected for 2D droplets at small Ca . For higher values of Ca , the numerical results deviate from the linear variation as the analytical solution is valid for the limit of small deformations.

We also perform tests for the deformation of a viscoelastic droplet with nondimensional numbers $Re = 0.3, Ca = 0.6, Wi = 0.4, \beta = 0.4$, and $Bi = 0$. Figure 17 (right panel) shows the deformation of the droplet over time. We compare the dynamics of the deformation with the computational solution previously presented by Figueiredo *et al.* [102], where a good agreement was observed.

Finally, we perform tests for an EVP droplet under shear. For a 3D droplet, this problem has been explored in [43], but in our validation test, we chose to perform 2D simulations

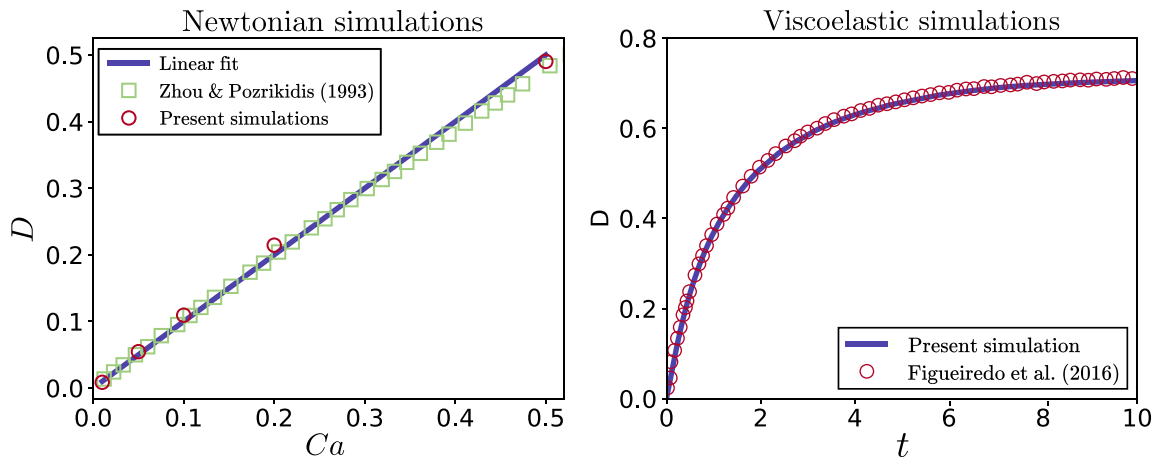


FIG. 17. Validation results for Newtonian and viscoelastic droplets under simple shear flow. (Left) Final deformation of a Newtonian droplet for different capillary numbers. (Right) Transient droplet deformation of a viscoelastic droplet under shear.

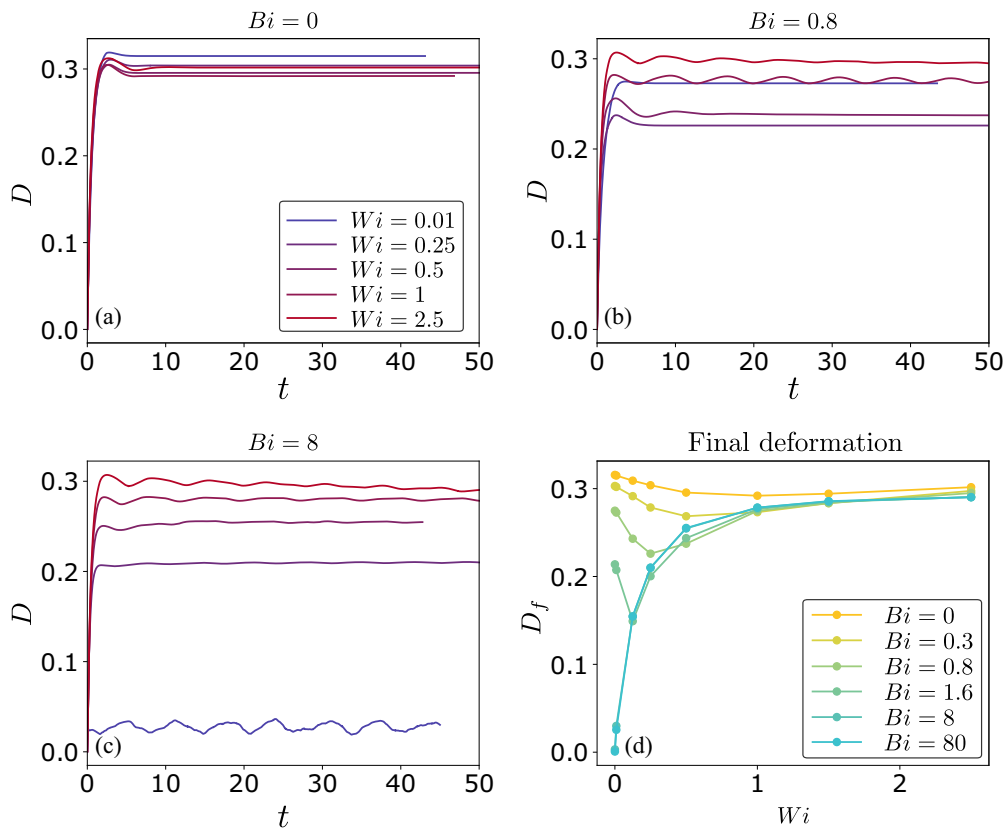


FIG. 18. Transient and steady-state deformation of an EVP droplet under shear for different Bingham and Weissenberg numbers. [(a)–(c)] Transient deformation for three different values of the Bingham number. (d) Final deformation for various Bi and Wi .

since our droplet spreading work is also a 2D (axisymmetric) problem. Figures 18(a)–18(c) show the evolution of the droplet deformation as a function of time for three different Bingham numbers. For each Bingham, a set of five Weissenberg numbers are explored. The transient behavior qualitatively compares well with those of [43], as we also see some temporary oscillations for cases with intermediate and high Wi . The final droplet deformation is shown in Fig. 18(d) for various Bi and Wi and, once again, good qualitative agreement is observed with [43]. For low values of Bi , we observe the non-monotonic influence of elasticity, where the deformation first decreases and then increases again with Wi . For high values of Bi , the deformation increases monotonically with Wi . We note that, quantitatively, our values of D are smaller than those of [43] due to the fact that they performed 3D droplet simulations, while the ones presented here are 2D.

4. Elastocapillarity

Figure 19 presents the data in Fig. 8 as a function of De . Note that the prefactors presented here are simply good fit through the data and are not from asymptotic analysis. A more rigorous analysis like those presented for viscoplastic limits [44] is needed to find the exact prefactors.

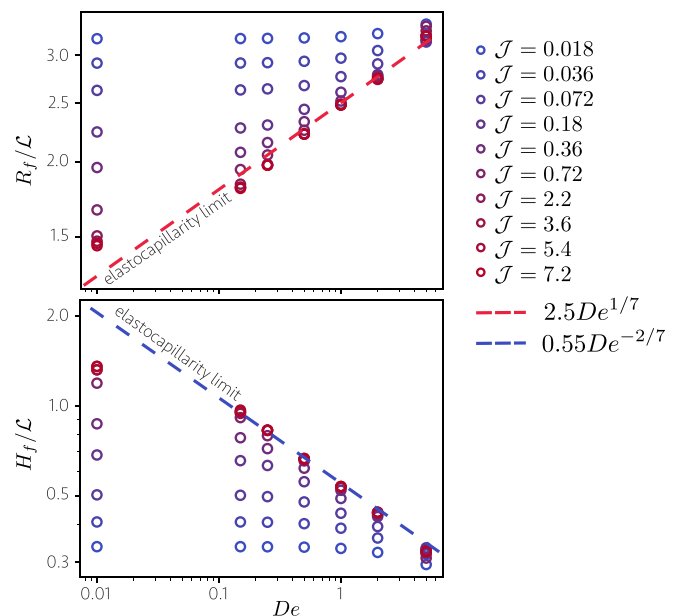


FIG. 19. Final radius and height as a function of De . The dashed lines show the scaling laws for the elastocapillarity limit, where both \mathcal{J} and De are high enough such that the droplet spreads and stops like a soft solid.

- [1] H. A. Barnes, The yield stress—A review or ‘πανταρει’ everything flows? *J. Nonnewton. Fluid Mech.* **81**, 133 (1999).
- [2] B. Derby, Inkjet printing of functional and structural materials: Fluid property requirements, feature stability, and resolution, *Annu. Rev. Mater. Res.* **40**, 395 (2010).
- [3] A. B. Thompson, C. R. Tipton, A. Juel, A. L. Hazel, and M. Dowling, Sequential deposition of overlapping droplets to form a liquid line, *J. Fluid Mech.* **761**, 261 (2014).
- [4] M. E. Mackay, The importance of rheological behavior in the additive manufacturing technique material extrusion, *J. Rheol.* **62**, 1549 (2018).
- [5] D. Lohse, Fundamental fluid dynamics challenges in inkjet printing, *Annu. Rev. Fluid Mech.* **54**, 349 (2022).
- [6] R. H. Ewoldt and C. Saengow, Designing complex fluids, *Annu. Rev. Fluid Mech.* **54**, 413 (2021).
- [7] L. Tanner, The spreading of silicone oil drops on horizontal surfaces, *J. Phys. D* **12**, 1473 (1979).
- [8] D. Bonn, J. Eggers, J. Indekeu, J. Meunier, and E. Rolley, Wetting and spreading, *Rev. Mod. Phys.* **81**, 739 (2009).
- [9] N. Bergemann, A. Juel, and M. Heil, Viscous drops on a layer of the same fluid: From sinking, wedging and spreading to their long-time evolution, *J. Fluid Mech.* **843**, 1 (2018).
- [10] M. Jalaal, C. Seyfert, and J. H. Snoeijer, Capillary ripples in thin viscous films, *J. Fluid Mech.* **880**, 430 (2019).
- [11] V. Bergeron, D. Bonn, J. Y. Martin, and L. Vovelle, Controlling droplet deposition with polymer additives, *Nature (London)* **405**, 772 (2000).
- [12] Y. Wang, D.-Q. Minh, and G. Amberg, Dynamic wetting of viscoelastic droplets, *Phys. Rev. E* **92**, 043002 (2015).
- [13] D. Izbassarov and M. Muradoglu, Effects of viscoelasticity on drop impact and spreading on a solid surface, *Phys. Rev. Fluids* **1**, 023302 (2016).
- [14] Y. Wang, M. Do-Quang, and G. Amberg, Impact of viscoelastic droplets, *J. Nonnewton. Fluid Mech.* **243**, 38 (2017).
- [15] B. Gorin, G. Di Mauro, D. Bonn, and H. Kellay, Universal aspects of droplet spreading dynamics in Newtonian and non-Newtonian fluids, *Langmuir* **38**, 2608 (2022).
- [16] L.-H. Luu and Y. Forterre, Drop impact of yield-stress fluids, *J. Fluid Mech.* **632**, 301 (2009).
- [17] A. Saïdi, C. Martin, and A. Magnin, Influence of yield stress on the fluid droplet impact control, *J. Nonnewton. Fluid Mech.* **165**, 596 (2010).
- [18] A. Saïdi, C. Martin, and A. Magnin, Effects of surface properties on the impact process of a yield stress fluid drop, *Exp. Fluids* **51**, 211 (2011).
- [19] B. C. Blackwell, M. E. Deetjen, J. E. Gaudio, and R. H. Ewoldt, Sticking and splashing in yield-stress fluid drop impacts on coated surfaces, *Phys. Fluids* **27**, 043101 (2015).
- [20] C. M. Oishi, F. P. Martins, and R. L. Thompson, The “avalanche effect” of an elasto-viscoplastic thixotropic material on an inclined plane, *J. Nonnewton. Fluid Mech.* **247**, 165 (2017).
- [21] S. Sen, A. G. Morales, and R. H. Ewoldt, Viscoplastic drop impact on thin films, *J. Fluid Mech.* **891**, A27 (2020).
- [22] C. M. Oishi, R. L. Thompson, and F. P. Martins, Impact of capillary drops of complex fluids on a solid surface, *Phys. Fluids* **31**, 123109 (2019).
- [23] G. Martouzet, L. Jørgensen, Y. Pelet, A.-L. Biance, and C. Barentin, Dynamic arrest during the spreading of a yield stress fluid drop, *Phys. Rev. Fluids* **6**, 044006 (2021).
- [24] O. D’Angelo, F. Kuthe, K. van Nieuwland, C. Ederveen Janssen, T. Voigtmann, and M. Jalaal, Spreading of droplets under various gravitational accelerations, *Rev. Sci. Instrum.* **93**, 115103 (2022).
- [25] J. van der Kolk, D. Tieman, and M. Jalaal, Viscoplastic lines: Printing a single filament of yield stress material on a surface, *J. Fluid Mech.* **958**, A34 (2023).
- [26] P. Saramito, A new constitutive equation for elastoviscoplastic fluid flows, *J. Nonnewton. Fluid Mech.* **145**, 1 (2007).
- [27] P. Saramito, A new elastoviscoplastic model based on the Herschel–Bulkley viscoplastic model, *J. Nonnewton. Fluid Mech.* **158**, 154 (2009).
- [28] P. R. de Souza Mendes, Thixotropic elasto-viscoplastic model for structured fluids, *Soft Matter* **7**, 2471 (2011).
- [29] C. J. Dimitriou and G. H. McKinley, A comprehensive constitutive law for waxy crude oil: A thixotropic yield stress fluid, *Soft Matter* **10**, 6619 (2014).
- [30] D. Fraggedakis, Y. Dimakopoulos, and J. Tsamopoulos, Yielding the yield stress analysis: A thorough comparison of recently proposed elasto-visco-plastic (EVP) fluid models, *J. Nonnewton. Fluid Mech.* **236**, 104 (2016).
- [31] P. Saramito and A. Wachs, Progress in numerical simulation of yield stress fluid flows, *Rheol. Acta* **56**, 211 (2017).
- [32] I. Cheddadi, P. Saramito, B. Dollet, C. Raufaste, and F. Graner, Understanding and predicting viscous, elastic, plastic flows, *Eurphys. J. E* **34**, 1 (2011).
- [33] D. Fraggedakis, Y. Dimakopoulos, and J. Tsamopoulos, Yielding the yield-stress analysis: a study focused on the effects of elasticity on the settling of a single spherical particle in simple yield-stress fluids, *Soft matter* **12**, 5378 (2016).
- [34] E. Chaparian, M. N. Ardekani, L. Brandt, and O. Tammisola, Particle migration in channel flow of an elastoviscoplastic fluid, *J. Nonnewton. Fluid Mech.* **284**, 104376 (2020).
- [35] B. Nassar, P. R. de Souza Mendes, and M. F. Naccache, Flow of elasto-viscoplastic liquids through an axisymmetric expansion–contraction, *J. Nonnewton. Fluid Mech.* **166**, 386 (2011).
- [36] D. Izbassarov, M. E. Rosti, L. Brandt, and O. Tammisola, Effect of finite Weissenberg number on turbulent channel flows of an elastoviscoplastic fluid, *J. Fluid Mech.* **927**, A45 (2021).
- [37] A. Kordalis, S. Varchanis, G. Ioannou, Y. Dimakopoulos, and J. Tsamopoulos, Investigation of the extensional properties of elasto-visco-plastic materials in cross-slot geometries, *J. Nonnewton. Fluid Mech.* **296**, 104627 (2021).
- [38] L. Duffo and S. Hormozi, Elastoviscoplastic flows in porous media, *J. Nonnewton. Fluid Mech.* **258**, 10 (2018).
- [39] E. Chaparian, D. Izbassarov, F. De Vita, L. Brandt, and O. Tammisola, Yield-stress fluids in porous media: A comparison of viscoplastic and elastoviscoplastic flows, *Meccanica* **55**, 331 (2020).
- [40] M. De Corato, B. Saint-Michel, G. Makrigiorgos, Y. Dimakopoulos, J. Tsamopoulos, and V. Garbin, Oscillations of small bubbles and medium yielding in elastoviscoplastic fluids, *Phys. Rev. Fluids* **4**, 073301 (2019).
- [41] P. Moschopoulos, A. Spyridakis, S. Varchanis, Y. Dimakopoulos, and J. Tsamopoulos, The concept of elasto-visco-plasticity and its application to a bubble rising in yield stress fluids, *J. Nonnewton. Fluid Mech.* **297**, 104670 (2021).

- [42] C. M. Oishi, R. L. Thompson, and F. P. Martins, Normal and oblique drop impact of yield stress fluids with thixotropic effects, *J. Fluid Mech.* **876**, 642 (2019).
- [43] D. Izbassarov and O. Tammisola, Dynamics of an elastoviscoplastic droplet in a newtonian medium under shear flow, *Phys. Rev. Fluids* **5**, 113301 (2020).
- [44] M. Jalaal, B. Stoeber, and N. J. Balmforth, Spreading of viscoplastic droplets, *J. Fluid Mech.* **914**, A21 (2021).
- [45] G. Tryggvason, R. Scardovelli, and S. Zaleski, *Direct Numerical Simulations of Gas-Liquid Multiphase Flows* (Cambridge University Press, Cambridge, 2011).
- [46] J. G. Oldroyd, On the formulation of rheological equations of state, *Proc. R. Soc. London A* **200**, 523 (1950).
- [47] H. A. Stone, M. J. Shelley, and E. Boyko, A note about convected time derivatives for flows of complex fluids, *Soft Matter* **19**, 5353 (2023).
- [48] J. H. Snoeijer, A. Pandey, M. A. Herrada, and J. Eggers, The relationship between viscoelasticity and elasticity, *Proc. R. Soc. A: Math. Phys. Engn. Sci.* **476**, 20200419 (2020).
- [49] E. C. Bingham, An investigation of the laws of plastic flow, No. 278, US Government Printing Office, 1917.
- [50] I. Frigaard, Simple yield stress fluids, *Curr. Opin. Colloid Interface Sci.* **43**, 80 (2019).
- [51] A. Morozov and S. E. Spagnolie, Introduction to complex fluids, in *Complex Fluids in Biological Systems: Experiment, Theory, and Computation* (Springer, New York, 2015), pp. 3–52.
- [52] J. Hinch and O. Harlen, Oldroyd B, and not A? *J. Nonnewton. Fluid Mech.* **298**, 104668 (2021).
- [53] N. Balmforth and R. Craster, Geophysical aspects of non-Newtonian fluid mechanics, in *Geomorphological Fluid Mechanics* (Springer-Verlag, Berlin, 2015), pp. 34–51.
- [54] C. Ancey, Plasticity and geophysical flows: A review, *J. Nonnewton. Fluid Mech.* **142**, 4 (2007).
- [55] C. Viezel, M. Tomé, F. Pinho, and S. McKee, An Oldroyd-B solver for vanishingly small values of the viscosity ratio: Application to unsteady free surface flows, *J. Nonnewton. Fluid Mech.* **285**, 104338 (2020).
- [56] G. H. McKinley, Visco-elasto-capillary thinning and break-up of complex fluids, *Rheology Reviews* (British Society of Rheology, Aberystwyth, 2005).
- [57] C. Clasen, J. Eggers, M. A. Fontelos, J. Li, and G. H. McKinley, The beads-on-string structure of viscoelastic threads, *J. Fluid Mech.* **556**, 283 (2006).
- [58] P. P. Bhat, S. Appathurai, M. T. Harris, M. Pasquali, G. H. McKinley, and O. A. Basaran, Formation of beads-on-a-string structures during break-up of viscoelastic filaments, *Nat. Phys.* **6**, 625 (2010).
- [59] A. Ardekani, V. Sharma, and G. McKinley, Dynamics of bead formation, filament thinning and breakup in weakly viscoelastic jets, *J. Fluid Mech.* **665**, 46 (2010).
- [60] A. Deblais, K. Velikov, and D. Bonn, Pearling instabilities of a viscoelastic thread, *Phys. Rev. Lett.* **120**, 194501 (2018).
- [61] M. Jalaal, Plastocapillarity, *Science Talks* **6**, 100232 (2023).
- [62] V. Sanjay, D. Lohse, and M. Jalaal, Bursting bubble in a viscoplastic medium, *J. Fluid Mech.* **922**, A2 (2021).
- [63] W. Thomson, On the elasticity and viscosity of metals, *Proc. R. Soc. London* **14**, 289 (1865).
- [64] W. Voigt, Ueber innere Reibung fester Körper, insbesondere der metalle, *Ann. Phys. (Leipzig)* **283**, 671 (1892).
- [65] R. S. Lakes, *Viscoelastic Solids*, Vol. 9 (CRC Press, Boca Raton, FL, 1998).
- [66] R. W. Style, A. Jagota, C.-Y. Hui, and E. R. Dufresne, Elastocapillarity: Surface tension and the mechanics of soft solids, *Annu. Rev. Condens. Matter Phys.* **8**, 99 (2017).
- [67] J. Bico, É. Reyssat, and B. Roman, Elastocapillarity: When surface tension deforms elastic solids, *Annu. Rev. Fluid Mech.* **50**, 629 (2018).
- [68] B. Andreotti and J. H. Snoeijer, Statics and dynamics of soft wetting, *Annu. Rev. Fluid Mech.* **52**, 285 (2020).
- [69] S. Popinet and Collaborators, Basilisk c, 2013–2021, Accessed on 01 01, 2024.
- [70] S. Popinet, Gerris: A tree-based adaptive solver for the incompressible euler equations in complex geometries, *J. Comput. Phys.* **190**, 572 (2003).
- [71] S. Popinet, An accurate adaptive solver for surface-tension-driven interfacial flows, *J. Comput. Phys.* **228**, 5838 (2009).
- [72] C. Hirt and B. Nichols, Volume of fluid (VOF) method for the dynamics of free boundaries, *J. Comput. Phys.* **39**, 201 (1981).
- [73] S. Popinet, A quadtree-adaptive multigrid solver for the Serre–Green–Naghdi equations, *J. Comput. Phys.* **302**, 336 (2015).
- [74] See Supplemental Material at <http://link.aps.org/supplemental/10.1103/PhysRevResearch.6.013226> for the simulation videos.
- [75] B. M. Rauzan, A. Z. Nelson, S. E. Lehman, R. H. Ewoldt, and R. G. Nuzzo, Particle-free emulsions for 3D printing elastomers, *Adv. Funct. Mater.* **28**, 1707032 (2018).
- [76] L. Friedrich and M. Begley, Corner accuracy in direct ink writing with support material, *Bioprinting* **19**, e00086 (2020).
- [77] M. Milazzo, V. Fitzpatrick, C. E. Owens, I. M. Carraretto, G. H. McKinley, D. L. Kaplan, and M. J. Buehler, 3D printability of silk/hydroxyapatite composites for microprosthetic applications, *ACS Biomater. Sci. Eng.* **9**, 1285 (2023).
- [78] E. García-Tuñón, R. Agrawal, B. Ling, and D. J. Dennis, Fourier-transform rheology and printability maps of complex fluids for three-dimensional printing, *Phys. Fluids* **35**, 017113 (2023).
- [79] M. Saadi, A. Maguire, N. T. Pottackal, M. S. H. Thakur, M. M. Ikram, A. J. Hart, P. M. Ajayan, and M. M. Rahman, Direct ink writing: A 3D printing technology for diverse materials, *Adv. Mater.* **34**, 2108855 (2022).
- [80] A. M. Afonso, P. J. Oliveira, F. T. Pinho, and M. A. Alves, Dynamics of high-Deborah-number entry flows: A numerical study, *J. Fluid Mech.* **677**, 272 (2011).
- [81] C. J. Dimitriou and G. H. McKinley, A canonical framework for modeling elasto-viscoplasticity in complex fluids, *J. Nonnewton. Fluid Mech.* **265**, 116 (2019).
- [82] K. Kamani, G. J. Donley, and S. A. Rogers, Unification of the rheological physics of yield stress fluids, *Phys. Rev. Lett.* **126**, 218002 (2021).
- [83] K. M. Kamani, G. J. Donley, R. Rao, A. M. Grillet, C. Roberts, A. Shetty, and S. A. Rogers, Understanding the transient large amplitude oscillatory shear behavior of yield stress fluids, *J. Rheol.* **67**, 331 (2023).
- [84] V. R. Kern, T. Sæter, and A. Carlson, Viscoplastic sessile drop coalescence, *Phys. Rev. Fluids* **7**, L081601 (2022).

- [85] P. J. Dekker, M. A. Hack, W. Tewes, C. Datt, A. Bouillant, and J. H. Snoeijer, When elasticity affects drop coalescence, *Phys. Rev. Lett.* **128**, 028004 (2022).
- [86] M. A. Fardin, M. Hautefeuille, and V. Sharma, Spreading, pinching, and coalescence: The Ohnesorge units, *Soft Matter* **18**, 3291 (2022).
- [87] A. T. Oratis, V. Bertin, and J. H. Snoeijer, Coalescence of bubbles in a viscoelastic liquid, [arXiv:2305.01363](https://arxiv.org/abs/2305.01363).
- [88] A. S. Rajput, S. C. Varma, and A. Kumar, Sub-newtonian coalescence in polymeric fluids, *Soft Matter* **19**, 4847 (2023).
- [89] F. Ingremeau and H. Kellay, Stretching polymers in droplet-pinch-off experiments, *Phys. Rev. X* **3**, 041002 (2013).
- [90] S. Rajesh, S. S. Peddada, V. Thiévenaz, and A. Sauret, Pinch-off of bubbles in a polymer solution, *J. Nonnewton. Fluid Mech.* **310**, 104921 (2022).
- [91] M. S. Sadullah, C. Semprebon, and H. Kusumaatmaja, Drop dynamics on liquid-infused surfaces: The role of the lubricant ridge, *Langmuir* **34**, 8112 (2018).
- [92] M. J. Kreder, D. Daniel, A. Tetreault, Z. Cao, B. Lemaire, J. V. I. Timonen, and J. Aizenberg, Film dynamics and lubricant depletion by droplets moving on lubricated surfaces, *Phys. Rev. X* **8**, 031053 (2018).
- [93] A. Pandey, B. Andreotti, S. Karpitschka, G. J. van Zwieten, E. H. van Brummelen, and J. H. Snoeijer, Singular nature of the elastocapillary ridge, *Phys. Rev. X* **10**, 031067 (2020).
- [94] J. Y. Kim, S. Heyden, D. Gerber, N. Bain, E. R. Dufresne, and R. W. Style, Measuring surface tensions of soft solids with huge contact-angle hysteresis, *Phys. Rev. X* **11**, 031004 (2021).
- [95] J. Mewis and N. J. Wagner, Thixotropy, *Adv. Colloid Interface Sci.* **147-148**, 214 (2009).
- [96] S. Sen, A. G. Morales, and R. H. Ewoldt, Thixotropy in viscoplastic drop impact on thin films, *Phys. Rev. Fluids* **6**, 043301 (2021).
- [97] T. C. Papanastasiou, Flows of materials with yield, *J. Rheol.* **31**, 385 (1987).
- [98] I. Frigaard and C. Nouar, On the usage of viscosity regularisation methods for visco-plastic fluid flow computation, *J. Nonnewton. Fluid Mech.* **127**, 1 (2005).
- [99] J. López-Herrera, S. Popinet, and A. Castrejón-Pita, An adaptive solver for viscoelastic incompressible two-phase problems applied to the study of the splashing of weakly viscoelastic droplets, *J. Nonnewton. Fluid Mech.* **264**, 144 (2019).
- [100] H. Franca, Elastoviscoplastic droplet spreading, https://github.com/FluidLab/EVP_droplet_spreading.
- [101] H. Zhou and C. Pozrikidis, The flow of suspensions in channels: Single files of drops, *Phys. Fluids* **5**, 311 (1993).
- [102] R. Figueiredo, C. Oishi, A. Afonso, I. Tasso, and J. Cuminato, A two-phase solver for complex fluids: Studies of the Weissenberg effect, *Int. J. Multiphase Flow* **84**, 98 (2016).